Improved visualization of gastrointestinal slow wave propagation using a novel wavefront-orientation interpolation technique

Terence P. Mayne, Niranchan Paskaranandavadivel, Jonathan C. Erickson, Gregory O'Grady, Leo K. Cheng, Timothy R. Angeli*

***Abstract*— *Objective:* High-resolution mapping of gastrointestinal (GI) slow waves is a valuable technique for research and clinical applications. Interpretation of high-resolution GI mapping data relies on animations of slow wave propagation, but current methods remain as rudimentary, pixelated electrode activation animations. This study aimed to develop improved methods of visualizing high-resolution slow wave recordings that increases ease of interpretation. *Methods:* The novel method of 'wavefront-orientation' interpolation was created to account for the planar movement of the slow wave wavefront, negate any need for distance calculations, remain robust in atypical wavefronts (i.e., dysrhythmias), and produce an appropriate interpolation boundary. The wavefront-orientation method determines the orthogonal wavefront direction and calculates interpolated values as the mean slow wave activation-time (AT) of the pair of linearly adjacent electrodes along that direction. Stairstep upsampling increased smoothness and clarity. *Results:* Animation accuracy of 17 human high-resolution slow wave recordings (64-256 electrodes) was verified by visual comparison to the prior method showing a clear improvement in wave smoothness that enabled more accurate interpretation of propagation, as confirmed by an assessment of clinical applicability performed by 8 GI clinicians. Quantitatively, the new method produced accurate interpolation values compared to experimental data (mean difference 0.02 ± 0.05 s) and was accurate when applied solely to dysrhythmic data (0.02 ± 0.06 s), both within the error in manual AT marking (mean 0.2 s). Mean interpolation processing time was 6.0 s per wave. *Conclusion & Significance:* These novel methods provide a validated visualization platform that will improve analysis of high-resolution GI mapping in research and clinical translation.**

Manuscript received June 6, 2017; revised Sept. 26, 2017; accepted Oct. 16, 2017. This work and/or authors were supported by the University of Auckland Faculty Research and Development Fund (FRDF), New Zealand Health Research Council (HRC), Medical Technologies Centre of Research Excellence (MedTech CoRE) New Zealand, and the U.S. National Institutes of Health (R01 DK64775). T. R. Angeli was supported by the Auckland Medical Research Foundation Edith C. Coan Fellowship.

T. P. Mayne and T. R. Angeli are with the Auckland Bioengineering Institute, University of Auckland, New Zealand (*correspondence e-mail: t.angeli@auckland.ac.nz). N. Paskaranandavadivel and G. O'Grady are with the Auckland Bioengineering Institute and Department of Surgery, University of Auckland, New Zealand. J. C. Erickson is with Washington and Lee University, Lexington, VA, USA. L. K. Cheng is with the Auckland Bioengineering Institute, University of Auckland, New Zealand, and Department of Surgery, Vanderbilt University, Nashville, TN, USA.

***Index Terms*—Animation, Wave interpolation, Bioelectrical, Electrophysiology, Stomach, Wave propagation.**

I. Introduction

GASTROINTESTINAL (GI) motility is governed in part by an underlying bioelectrical activity termed slow waves [1]. The contractions that underpin digestion are coordinated by the spatiotemporal properties of these slow waves that propagate along the GI tract. Gastric slow waves originate from a single pacemaker region and rapidly establish planar ring wavefronts that propagate down the stomach [2]. The recent development of high-resolution GI mapping is significantly expanding the understanding of slow wave dynamics through simultaneous recordings of slow wave activity from dense arrays of many electrodes [3], [4]. High-resolution mapping has fueled clinical interest in slow wave dynamics through recent descriptions of spatially-complex propagation abnormalities (dysrhythmias) in patients with functional gastric disorders [5], [6], and holds potential as a clinical diagnostic method.

Accurate visualization of slow wave activity is critical to the understanding, diagnosis, and therapeutic potential of abnormal GI activity. Several visualization tools are currently used for defining slow wave activity, including static isochronal activation-time (AT) maps that show propagation of a single slow wave as a color map, and animations of the ATs across the electrode array [7], [8]. However, animations to date have been simplistic, representing each electrode as an individual square and lacking interpolation of propagation between electrode locations. These existing animation methods result in a basic, pixelated visualization that does not accurately represent inter-electrode wavefront behavior. Missing data (e.g., due to incomplete electrode contact) and complex wavefront interactions, may also be incorrectly represented or communicated by these existing methods. An improved method for realistically visualizing slow wave propagation, including an accurate interpolation technique, is therefore needed for both research interpretations and clinical translation of GI mapping.

Wavefront interpolation algorithms have been adapted for highly specific conduction mediums and wave sources in other fields [9]–[11]. Cardiac wavefront interpolation studies have used eikonal-diffusion, but that method is complex and

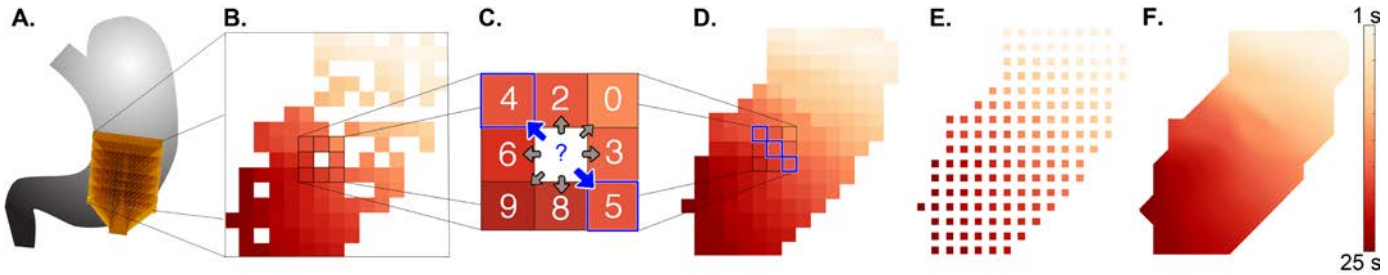

Fig. 1. Interpolation pipeline to transform original data to smoothed wavefront maps for subsequent animation. Maps represent slow wave ATs across the electrode array from earlier (light orange) to later (dark red) time points. **A)** Schematic of electrode grid placed on stomach to record slow waves. **B)** An example of experimental AT data containing missing values (white). **C)** Nine electrodes where the center value is the interpolation target, with illustrative ATs overlaid on the neighbors. The interpolation method detects the wavefront-orientation by identifying the pair of linearly adjacent neighbors (i.e., horizontal, vertical, and diagonal pairs) with the minimum difference in ATs. In this example, the left-right diagonal pair identified with blue arrows is the linear pair with the closest ATs (4 s, 5 s) and determines that the wavefront is approximately left-right diagonally oriented, resulting in a mean interpolated value of 4.5 s. **D)** Fully interpolated AT map of the raw data. **E)** A single step of upsampling. **F)** 6 iterations of stairstep interpolation produces a comprehensive wavefront AT map ready to be converted to animation.

requires an additional boundary condition and specified conduction properties, making it non-ideal for GI slow waves [10], [12]. A recent planar wavefront interpolation study in the field of optics demonstrated that linear interpolation is an effective method for reducing error and computation-time [9], and it has been shown that interpolation error can be reduced in two-dimensional datasets containing multiple inflection points by selecting only those neighbors nearest to the interpolation target [11], which is applicable to the velocity variations present in dysrhythmic slow waves [13].

The aims of this study were therefore to develop and validate methods that produce smoothed and accurate animations of high-resolution slow wave recordings by developing algorithms that: (1) upsample resolution of slow wave animations; (2) account for the localized planar nature of the slow wave wavefront; (3) simulate the trailing edge of the slow wave; (4) limit error by confining interpolation to regions with reliable neighboring data; (5) accurately represent the recorded data in normal and dysrhythmic slow waves containing velocity variances.

II. Methods

The development of an improved animation algorithm first necessitated a robust interpolation method to calculate ATs at: (1) electrodes missing experimental data, and (2) newly inserted data-points during upsampling. Additionally, a large clinically-relevant dataset of experimental test cases was needed, including both normal and dysrhythmic slow waves.

A. Overview of Wavefront-Orientation Interpolation

AT data points represent the arrival of the slow wave wavefront at each electrode. To interpolate an unknown AT point, the time that the wavefront reaches that electrode is estimated. The theoretical basis of wavefront-orientation interpolation considers that the slow wave wavefront propagates in an approximately planar orientation with neighboring wavefront ATs that are closely synchronized. Therefore, the most representative and subsequently computationally-effective neighbors to derive an interpolated value from are the linear adjacent neighbor pair that is most closely oriented to that of the wavefront. The linear pairs that intersect directly at the target (diagonal, vertical or horizontal pairs) and are most similar in wavefront AT are selected to estimate the wavefront arrival and interpolate the missing value (Fig. 1C). The mean of the ATs of the selected pair provides a linear estimation of the missing AT value based on the wavefront orientation. This method of interpolation is computationally efficient because the linear electrode pairs are always equidistant to the target for a regularly-spaced electrode array; distance and speed calculations are thereby unnecessary.

For additional robustness, the algorithm sequences the interpolation points from most to least number of 'good neighbors' (*i.e.*, data points with valid ATs that were either experimentally marked or interpolated). The pool of neighbor data is thereby maximized to increase interpolation accuracy.

Stairstep upsampling then inserts alternating rows and columns of empty data cells. Wavefront-orientation interpolation is re-applied throughout upsampling to maintain the wavefront dynamics inherent to the experimental data that are identified at the electrode interpolation level and thereby reduce discretization error (Fig. 1D-F).

B. Wavefront-Orientation Interpolation Algorithm

Consider a regularly spaced electrode array of dimensions $m \times n$ for a single recorded slow wave cycle containing measured ATs. At sites where no AT was recorded the value is set to 'unknown'. These missing data sites are the targets for interpolation.

For each unknown data point, the number of neighbors with valid AT values, termed 'good neighbors', is counted and represented by g. G contains the matrix of good neighbors for sites at which ATs are missing. X represents the subset of electrode sites from the electrode grid with missing AT values $x_{m,n}$, where the number of good neighbors at point (m, n) is $g_{m,n}$. Electrode sites in X are interpolated in order of descending g with a lower limit of ≥ 2. Thus points are sequenced from most to least number of good neighbors for interpolation.

For each interpolation target a 3×3 sub-matrix $u_{m,n}$ is constructed from the electrode grid such that the interpolation target is centrally positioned. The missing value is computed per Equation 1. The linearly-adjacent neighboring pair with the smallest time difference is averaged to calculate the interpolated value (Fig. 1B and 1C).

$$x_{m,n} = min\{\sum_{l=1}^{4} \Delta t(u_{m,n} * K_l)\} \quad (1)$$

Where K_l is the kernel used to compute Δt with $l = \{1, 2, 3, 4\}$ representing the label for the left-right diagonal, right-left diagonal, horizontal and vertical linear pairs.

If an AT for either neighbor of a pair is missing, no time difference is returned for that pair. If all pairs fail to return AT differences, interpolation fails for the target and the next unknown in the sequence is interpolated (*i.e.*, interpolation requires a minimum of one linearly adjacent pair of valid ATs). After all targets have had interpolation attempted, the algorithm is repeated with only those that failed because some of the previously missing pairs may now have been assigned a value. If interpolation still fails for $x_{m,n}$ it is removed from X and remains unknown. The requirement for an interpolation target to possess at least one linearly adjacent pair with valid ATs creates an automated and robust interpolation boundary.

C. Upsampling

To increase the precision of the image and reduce discretization error, single columns and rows of unknowns are added in each upsampling step to double the resolution of the image. This upsampling step is repeated with the interpolation described above in a stairstep fashion (i.e., repeated 1-fold increases in dimension followed by interpolation), and can be iterated to user preference.

D. High-Resolution Mapping Data

Previously recorded high-resolution mapping data of gastric slow wave activity was used to develop and validate the new animation algorithms [5], [6], [14]. This high-resolution mapping data was acquired intra-operatively using flexible-printed-circuit electrode arrays (64-256 electrodes; 4 mm inter-electrode spacing; 8-36 cm^2 array) placed directly on the gastric serosa [4]. Signals were acquired using a passive ActiveTwo system (Biosemi, Amsterdam, Netherlands).

The validation dataset for this study encompassed 17 recordings that included a total of 96 individual slow wave cycles, across 14 patients. 8 of the patients had healthy stomachs (4 undergoing surgery for abdominal malignancies not involving the GI tract [14]; 4 undergoing obesity surgery [15]). The remaining 6 patients had been diagnosed with functional GI disorders associated with slow wave dysrhythmias (3 diagnosed with gastroparesis [6]; 3 diagnosed with chronic unexplained nausea and vomiting [5]). These data thereby encompassed both normal and dysrhythmic slow wave propagation, enabling robust test cases for the algorithm development. Slow wave activity was analyzed in GEMS v1.5 [7], including the automated identification and grouping of ATs into wavefronts with manual review to ensure accuracy [16], [17]. ATs at each electrode location were exported as a matrix for each slow wave and passed into the subsequent visualization steps.

E. Interpolation of High-Resolution Mapping Dataset

The wavefront-orientation interpolation algorithm described above was applied to the validation dataset of 96 slow wave cycles. Interpolation was conducted with a resolution multiplier of 2-fold to 6-fold for accuracy validation. A 6-fold interpolation was used for published animations, figures, and computation-time calculations.

F. Validation using Inverted Interpolation

Inverted interpolation was performed to quantitatively validate the interpolation. That is, post-interpolation the original known AT values were removed, and the interpolation algorithms were applied to the inverted data (Fig. 2) [18].

Fig. 2. Validation pipeline of the interpolation using an inverted- interpolation of a slow wave AT map. This pipeline produces an accuracy value of the wavefront-orientation interpolation method. **A)** Original un-interpolated experimental data after a single upsampling. **B)** After interpolation, the original data (i.e., *A*) was removed to leave only the interpolated data points shown here. **C)** The original data sites were then re-interpolated. **D)** The interpolation error was calculated as the absolute value of the difference between the experimental data (*A)* and the re-interpolation of those data (*C)*.

G. Processing Time of Wavefront-Orientation Interpolation

The computational cost of wavefront-orientation interpolation was measured using the time taken to interpolate the validation dataset of 96 total slow wave cycles and the average interpolation time per wave was calculated. Interpolation processing was performed on an Intel Core i5 2GHz. Time was measured for 5-fold and 6-fold increases in resolution.

H. Animation

The interpolated AT 2D matrix was expanded to 3D by an added time dimension at 0.1 s per frame. All elements were set to 0, except in their active time frame they were set to 1. To simulate the slow wave trailing edge (i.e., recovery time window), a Gaussian filter with a sigma value of 12 was applied to the time dimension in a retrograde fashion to fade the slow waves over approximately 4.2 seconds, representing a constant activation-recovery period consistent with physiological averages [19], [20]. Slow wave matrices were merged in time and accounted for multiple slow wave cycles appearing in the same activation-time window. Intensity values were normalized (0 to 1) and a fourth dimension added to enable overlays of RGB colors. Electrodes were represented as overlaid dots that were color-coded to signify known ATs, unknown ATs, and currently 'activated' electrodes time-synced to the original, un-interpolated AT data (Figs. 3 and 4). The final animation was rendered using matplotlib 1.5.3 at 50 frames per second [21].

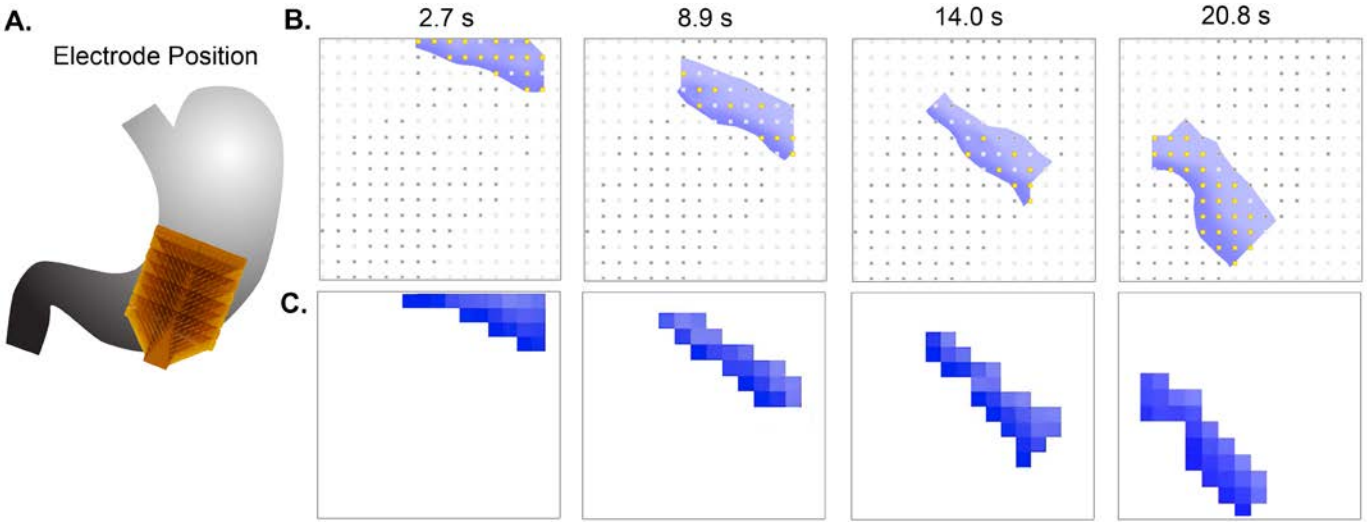

Fig. 3. Normal slow wave propagation - comparison of new wavefront-orientation slow wave animation versus previous pixelated GEMS animation of normal slow wave propagation of the same slow wave recording. **A)** Electrode array position. **B)** Frames from a slow wave animation generated by the new wavefront-orientation method. Black dots represent electrodes with known, recorded ATs and illuminate yellow on activation according to the raw, un-interpolated data. Light gray dots represent electrodes where no ATs were recorded. The slow wave is colored blue to represent normal propagation. **C)** Frames from a previous GEMS pixelated animation method of the same slow wave recording as *B*, where each square represents an electrode. See also Supplementary Animation 1.

I. Assessment of Clinical Applicability

GI clinicians were invited to complete a survey to assess the ease of interpretation and clinical applicability of the new animation method versus the previous pixelated GEMS animation method. Slow wave propagation patterns (n = 4) were presented to the clinicians, encompassing the same data included in Fig. 3 and Fig. 4 (Supplementary Animations 1-4). Each propagation sequence was presented simultaneously in side-by-side panels with one panel showing the new animation method and the other panel showing the previous GEMS animation method, presented in a counterbalanced fashion to prevent order bias. Clinicians were blinded to the animation type (*i.e.*, were not told which animation was new vs. previous GEMS method), and were asked to use a 5-point Likert scale to rank the 'ease of interpretation' (1 = uninterpretable, 5 = clear and obvious) and 'applicability to clinical assessment' (1 = not useful, 5 = extremely useful) of each animation. Clinicians were also asked 'which animation provides more information about the wavefront propagation', 'which animation would you prefer to use for interpretation', and for general comment on the animation methods.

Likert scale rankings were compared between the new animation method vs. the previous GEMS method using paired Student's t-test with significance threshold of $P < 0.05$.

III. Results

A. Animations

Animations were viewed across the 17 datasets and compared with the previous pixelated style of animations rendered in GEMS (Figs. 3 and 4). Visual comparison of slow wave activation patterns showed improvement in the precision of the wavefront edge using the new methods across both normal (Fig. 3; Supplementary Animation 1) and dysrhythmic cases (Fig. 4; Supplementary Animations 2-4). The new animations presented slow wave propagation data as continuous wavefronts with fading color intensity representing a typical slow wave recovery period [19], and electrode data as color-coded dots. The slow wave wavefront was accurately represented as a continuous wavefront by the newly developed animation methods, displaying a coherent wavefront orientation that presented an obvious and substantial improvement over the previous pixelated animations.

Computationally, the animation rendering and compression took a mean of 774 s per dataset, which equated to 137 s per wave.

B. Interpolation Validation

The wavefront-orientation interpolation method was accurate compared to experimental values with a mean difference across all waves of 0.02 ± 0.05 s for the 6-fold increase in resolution used for final animations. Interpolation accuracy increased with each stairstep interpolation iteration such that the mean difference between experimental data and re-interpolated values decreased by about 50% for each successive iteration (Fig. 5; n = 7856; 0.17 ± 0.23 s for 2-fold interpolation; 0.09 ± 0.13 s for 3-fold; 0.05 ± 0.08 s for 4-fold; 0.03 ± 0.06 s for 5-fold; 0.02 ± 0.05 s for 6-fold; 0.01 ± 0.05 s for 7-fold). Importantly, the mean difference for 6-fold interpolation is well within the level of accuracy found in manual marking of slow waves (mean 0.2 s; [16]).

Wavefront-orientation interpolation was designed to be computationally efficient; therefore, interpolation time was assessed across the validation dataset of 96 slow wave cycles.

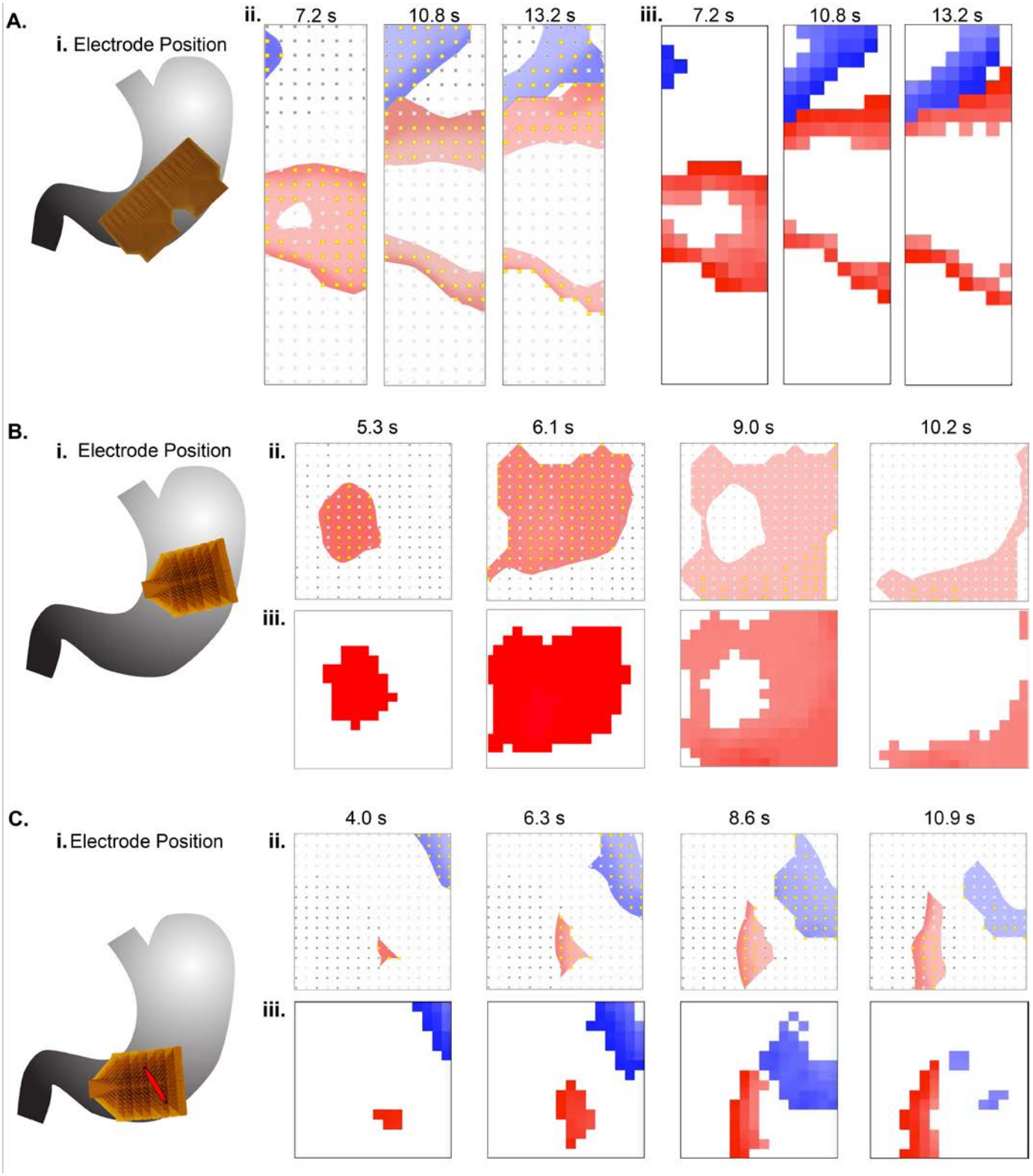

Fig. 4. Dysrhythmic slow wave propagation - comparison of new wavefront-orientation slow wave animations versus previous pixelated GEMS animations of dysrhythmic slow wave propagation, including: **A) stable ectopic pacemaker** resulting in secondary circumferential and retrograde propagation, which collides with a dissociated antegrade propagating wavefront (see also Supplementary Animation 2); **B) unstable ectopic pacemaker** resulting in circumferential and retrograde propagation, with regions of abnormally high (upper portion of mapped area) and low velocity (lower-left portion of mapped area; see also Supplementary Animation 3); **C) conduction block** of normal antegrade wavefront induced by surgical punch-biopsy in the middle of the array, resulting in a breakout ectopic pacemaker immediately distal to the block with rapid circumferential propagation (see also Supplementary Animation 4). Regions of dysrhythmic slow wave propagation are colored red, while regions of normal slow wave propagation are colored blue (color choice is a manually-selected parameter). Each example includes: **i)** Electrode position diagram. **ii)** Frames from a slow wave animation generated by the new wavefront-orientation method. Black dots represent electrodes with known, recorded ATs and illuminate yellow on activation according to the raw, un-interpolated data. Light gray dots represent electrodes where no ATs were recorded. **iii)** Frames from a previous GEMS pixelated animation method for comparison, where each square represents an electrode.

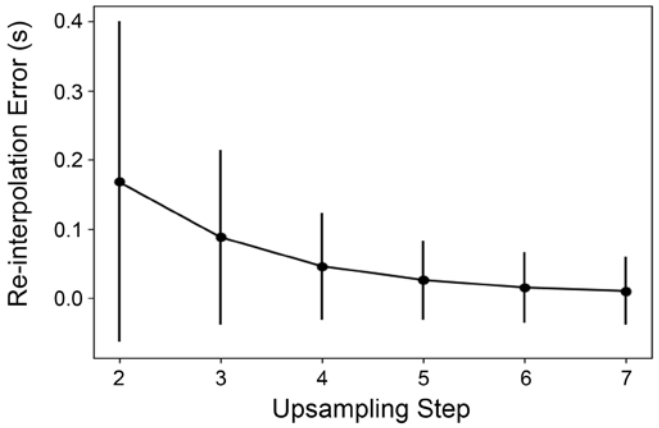

Fig. 5. Re-interpolation error for each successive upsampling step from 2-fold interpolation to 7-fold interpolation, demonstrating the successive decrease in re-interpolation error approaching a plateau at 6-fold interpolation.

The average interpolation time was 6.0s per slow wave for 6-fold increases in resolution.

C. Dysrhythmic Slow Wave Propagation

The animation and interpolation algorithms were applied to recordings of both normal and dysrhythmic slow wave propagation. Normal slow wave propagation is uniform and cohesive, and was therefore straight-forward for accurate, successful interpolation and animation of all recordings (Fig. 3; Supplementary Animation 1). The non-uniform, variable dysrhythmic propagation presented more challenging test-cases for the algorithms.

The newly developed animation and interpolation algorithms were applied to 11 recordings of dysrhythmic slow wave propagation, which included examples of each of the following established gastric dysrhythmia classifications [5], [6], [22]: stable ectopic pacemakers (present in n = 5 recordings), unstable ectopic pacemakers (n = 2), retrograde propagation (n = 7), circumferential propagation (n = 11), wavefront collisions (n = 4), abnormal velocity (n = 4), re-entry (n = 1), and conduction blocks (n = 6). As shown in Figure 4, the algorithms accurately interpolated and animated the stable and unstable ectopic pacemakers, retrograde and circumferential propagation, abnormal velocity, wavefront collisions, and conduction blocks that spanned more than one electrode width (i.e., wider than 4 mm). The animations of these dysrhythmias accurately presented continuous wavefronts with coherent orientation, representing an apparent and substantial improvement over the previous pixelated animations and thereby making these dysrhythmic propagation sequences more intuitive to accurately interpret (Fig. 4; Supplementary Animations 2-4). However, the algorithms incorrectly interpolated across conduction blocks that were one electrode wide or narrower (i.e., manifested as a single row of unknown in the high-resolution mapping data), representing these narrow conduction blocks as regions of slow conduction rather than complete block, which was also an issue with the previous pixelated animation methods.

The wavefront-orientation interpolation method was accurate when compared to experimental values of only dysrhythmic slow wave activity, with a mean difference of 0.02 ± 0.06 s between experimental and inverted-interpolation values (e.g., Fig. 2) for a 6-fold increase.

D. Assessment of Clinical Applicability

Assessment was performed by 8 GI clinicians, with clinical experience levels ranging from Trainee to Consultant Surgeon with over 30 years of experience, and assessment comprised 32 total comparisons (each of the 8 clinicians assessed all 4 animations). Results showed that the new visualization method was clinically preferred compared to the previous GEMS method across all assessed rankings and questions. The new method was rated as easier to interpret with a mean difference in Likert score of 1.0 (4.7 ± 0.5 vs. 3.7 ± 0.9; P < 0.001), and more applicable to clinical assessment with a mean difference in Likert score of 1.3 (4.8 ± 0.5 vs. 3.4 ± 0.8; P < 0.001). Clinicians also reported that the new animation method provided more information about the wavefront propagation in 21 of the 32 total comparisons (vs. 0 of 32 for the previous GEMS method, with 11 of 32 reporting no difference), and that the new method was preferred for clinical interpretation in 29 of the 32 comparisons (vs. 1 of 32 for the previous GEMS method, with 2 of 32 reporting no difference).

IV. Discussion

In this study, new methods were developed to interpolate and visualize gastric slow wave propagation data obtained through high-resolution bioelectrical mapping. These methods accurately interpolated missing data points in the experimental recordings using a robust algorithm that accounts for the localized planar wavefront inherent in both normal and dysrhythmic propagation, while remaining computationally efficient. The animations produced increased precision of the wavefront edge that remained correlated with the original experimental data. Importantly, these animation methods were able to accurately represent the range of dysrhythmias observed in functional GI disorders and resulting from surgical intervention [5], [6], [23], and were deemed to offer superior interpretation of GI slow wave propagation by GI clinicians, compared to previous animation methods.

A range of existing interpolation methods have been previously published, but were designed for non-GI fields (e.g., optics [9] and cardiology [10], [12]) with distinct conduction mediums and wave propagation characteristics that were not directly applicable to slow wave propagation. Therefore, we developed a robust method that accounts for the localized planar dynamics of gastric slow wave by constraining interpolation to the pair of adjacent neighbors that were closest in activation time and thereby most closely oriented to the direction of the wavefront. This method of interpolating across only the directly adjacent neighbors of the interpolation target was not only robust and accurate, but also negated the need for distance calculations because of the regularly-spaced electrode array, making it computationally efficient and enabling significantly higher resolutions with minimal computational cost. Additionally, this method of interpolation featured decreased error (increased accuracy) with each successive upsampling, further validating the method as an accurate means by which to increase the quality

of visualizing slow wave propagation. The increased accuracy of the successive upsampling and interpolation is likely due to the minimization of spatial discretization error, whereby the increased spatial resolution of the animations yields a better fit of the interpolated data to the actual wavefront orientation.

A significant benefit of the new interpolation method presented in this study is the production of an objective and visible indicator of inter-electrode slow wave propagation. The current high-resolution electrode arrays have an electrode size of 0.07 mm^2 (0.3 mm diameter circular contact) with 4 mm inter-electrode spacing [4]–[6]. The previous pixelated animation method was essentially up-scaling the electrodes to an effective area of 16 mm^2 by representing them as squares that fill the entire area of the electrode array without representing the inter-electrode space, nor interpolating the activity within that space [7]. The new methods at 6-fold interpolation more accurately approximate the effective electrode size as 0.06 mm^2 and interpolate the surrounding activity in the inter-electrode space, thereby providing increased information that may help the interpretation of gastric slow wave propagation, particularly in cases of dysrhythmias where propagation is non-uniform [5], [6], [15]. This was confirmed by the clinical applicability assessment and in additional comments by two clinicians who said that the increased resolution and plotting of electrodes provide "extra information" and "confidence" when interpreting wavefront propagation. Another clinician specifically remarked that the wavefront edge was more discernible.

The methods developed in this study accurately interpolated and visualized all dysrhythmic test cases based on established gastric dysrhythmia classifications [5], [22], except for narrow conduction blocks spanning a single electrode width or less, which were presented as regions of slow conduction instead of complete block. This limitation was not surprising, and resulted from the algorithm interpolating across single unknown data points (i.e., a single electrode) irrespective of changes in the speed of the wave. In the future, an additional method of detecting and visualizing conduction blocks would be complimentary to the animation and interpolation algorithms presented in this paper. Importantly, our new interpolation method is sensitive to changes in velocity, as are seen at sites of conduction block, thereby enabling possible extension of these methods to detect conduction blocks using a velocity-threshold technique [24], [25] and/or a curvature-based technique [26].

The algorithms developed in this study were limited to gastric data obtained from 2-dimensional (2D) electrode arrays with uniform electrode spacing, applied via open surgery [5], [6], [23]. Minimally-invasive methods of endoscopic and laparoscopic mapping hold great promise as a diagnostic tool for gastric dysrhythmias, but endoscopic mapping employs non-uniform, 3D electrode arrays [27], and some laparoscopic approaches also use non-uniform arrays [28]. The principles and techniques developed in this study could likely be adapted in future for application to non-uniform and 3D electrode arrays, intestinal slow wave propagation [29]–[31], and spike propagation [32], [33].

V. Conclusion

This study presents improved methods for visualizing and interpolating high-resolution gastric electrical mapping data that substantially enhance the presentation, accuracy, and interpretation of slow wave propagation. The newly-developed wavefront-orientation algorithm enables accurate, computationally-efficient interpolation of unknown data points based on physiologically-relevant wavefront propagation. These methods upsample the data to a resolution that accords with the realistic electrode size and accurately interpolates propagation in the inter-electrode space. Importantly, the methods developed in this study were validated across experimental datasets from healthy and diseased human patients, demonstrating vastly improved animations of both normal and dysrhythmic slow wave propagation and thereby improving the interpretation of these clinical data. This work now offers the potential for translation of these innovative methods to other research fields and into clinical application, for example to visualize diagnostic mapping data.

Acknowledgment

The authors thank Dr. Peng Du and the clinical staffs at Auckland City Hospital and the University of Mississippi Medical Center for their support with this study.

Conflicts of Interest

Authors TRA, NP, JCE, GOG, and LKC hold intellectual property in the field of gastric electrophysiology and are shareholders in FlexiMap. TPM declares no conflicts of interest. No commercial financial support was received for this study.

References

[1] J. D. Huizinga and W. J. E. P. Lammers, "Gut peristalsis is governed by a multitude of cooperating mechanisms," *Am. J. Physiol. Gastrointest. Liver Physiol.*, vol. 296, pp. G1-8, Jan. 2009.

[2] T. R. Angeli, G. O'Grady, and W. J. E. P. Lammers, "The electrical regulation of gastrointestinal motility at the whole-organ level," in *New advances in gastrointestinal motility research*, vol. 10, L. K. Cheng, A. J. Pullan, and G. Farrugia, Eds. Dordrecht: Springer Netherlands, 2013, pp. 95–112.

[3] W. J. E. P. Lammers, A. Al-Kais, S. Singh, K. Arafat, and T. Y. El-Sharkawy, "Multielectrode mapping of slow-wave activity in the isolated rabbit duodenum," *J. Appl. Phys.*, vol. 74, no. 3, pp. 1454–1461, Mar. 1993.

[4] P. Du, G. O'Grady, J. U. Egbuji, W. J. E. P. Lammers, D. Budgett, P. Nielsen, J. A. Windsor, A. J. Pullan, and L. K. Cheng, "High-resolution mapping of in vivo gastrointestinal slow wave activity using flexible printed circuit board electrodes: methodology and validation," *Ann. Biomed. Eng.*, vol. 37, no. 4, pp. 839–846, 2009.

[5] T. R. Angeli, L. K. Cheng, P. Du, T. H.-H. Wang, C. E. Bernard, M.-G. Vannucchi, M. S. Faussone-Pellegrini, C. Lahr, R. Vather, J. A. Windsor, G.

Farrugia, T. L. Abell, and G. O'Grady, "Loss of interstitial cells of Cajal and patterns of gastric dysrhythmia in patients with chronic unexplained nausea and vomiting," *Gastroenterology*, vol. 149, no. 1, p. 56–66.e5, 2015.

[6] G. O'Grady, T. R. Angeli, P. Du, C. Lahr, W. J. E. P. Lammers, J. A. Windsor, T. L. Abell, G. Farrugia, A. J. Pullan, and L. K. Cheng, "Abnormal initiation and conduction of slow-wave activity in gastroparesis, defined by high-resolution electrical mapping," *Gastroenterology*, vol. 143, no. 3, pp. 589-598–3, Sep. 2012.

[7] R. Yassi, G. O'Grady, N. Paskaranandavadivel, P. Du, T. R. Angeli, A. J. Pullan, L. K. Cheng, and J. C. Erickson, "The gastrointestinal electrical mapping suite (GEMS): software for analyzing and visualizing high-resolution (multi-electrode) recordings in spatiotemporal detail," *BMC Gastroenterol.*, vol. 12, no. 1, p. 60, Jan. 2012.

[8] N. Paskaranandavadivel, G. O. Grady, and L. K. Cheng, "Time delay mapping of high-resolution gastric slow wave activity," *IEEE Trans. Biomed. Eng.*, vol. 64, no. 1, pp. 166–172, 2017.

[9] T. Muroi, N. Kinoshita, N. Ishii, K. Kamijo, Y. Kawata, and H. Kikuchi, "Optical compensation for hologram distortion using wavefront interpolation in angle-multiplexed holograms," *J. Mod. Opt.*, vol. 61, no. 9, pp. 746–754, 2014.

[10] V. Jacquemet, "An eikonal-diffusion solver and its application to the interpolation and the simulation of reentrant cardiac activations," *Comput. Methods Programs Biomed.*, vol. 108, no. 2, pp. 548–558, 2012.

[11] D. Shepard, "A two-dimensional interpolation function for irregularly-spaced data," in *Conf. Proc. Assoc. Comput. Mach.*, 1968, pp. 517–524.

[12] K. A. Tomlinson, P. J. Hunter, and A. J. Pullan, "A Finite Element Method for an Eikonal Equation Model of Myocardial Excitation Wavefront Propagation," *SIAM J. Appl. Math.*, vol. 63, no. 1, pp. 324–350, 2002.

[13] G. O'Grady, P. Du, N. Paskaranandavadivel, T. R. Angeli, W. J. E. P. Lammers, S. J. Asirvatham, J. A. Windsor, G. Farrugia, A. J. Pullan, and L. K. Cheng, "Rapid high-amplitude circumferential slow wave propagation during normal gastric pacemaking and dysrhythmias," *Neurogastroenterol. Motil.*, vol. 24, no. 7, pp. e299-312, Jul. 2012.

[14] R. Berry, T. Miyagawa, N. Paskaranandavadivel, P. Du, T. R. Angeli, M. L. Trew, J. A. Windsor, Y. Imai, G. O'Grady, and L. K. Cheng, "Functional physiology of the human terminal antrum defined by high-resolution electrical mapping and computational modeling," *Am. J. Physiol. Gastrointest. Liver Physiol.*, vol. 311, no. 5, pp. G895–G902, 2016.

[15] R. Berry, L. K. Cheng, P. Du, N. Paskaranandavadivel, T. R. Angeli, T. Mayne, G. Beban, and G. O'Grady, "Patterns of abnormal gastric pacemaking after sleeve gastrectomy defined by laparoscopic high-resolution electrical mapping," *Obes. Surg.*, vol. 27, no. 8, pp. 1929–1937, 2017.

[16] J. C. Erickson, G. O'Grady, P. Du, C. Obioha, W. Qiao, W. O. Richards, L. A. Bradshaw, A. J. Pullan, and L. K. Cheng, "Falling-edge, variable threshold (FEVT) method for the automated detection of gastric slow wave events in high-resolution serosal electrode recordings," *Ann. Biomed. Eng.*, vol. 38, no. 4, pp. 1511–1529, Apr. 2010.

[17] J. C. Erickson, G. O'Grady, P. Du, J. U. Egbuji, A. J. Pullan, and L. K. Cheng, "Automated gastric slow wave cycle partitioning and visualization for high-resolution activation time maps," *Ann. Biomed. Eng.*, vol. 39, no. 1, pp. 469–483, Jan. 2011.

[18] M. Tomczak, "Spatial interpolation and its uncertainty using automated anisotropic inverse distance weighting (IDW) - cross-validation/jackknife approach," *J. Geogr. Inform. Decis. Anal.*, vol. 2, no. 2, pp. 18–30, 1998.

[19] N. Paskaranandavadivel, X. Pan, P. Du, G. O'Grady, and L. K. Cheng, "Detection of the recovery phase of in vivo gastric slow wave recordings," *Conf. Proc. IEEE. Eng. Med. Biol. Soc.*, vol. 1, pp. 6094–6097, 2015.

[20] N. Paskaranandavadivel, L. K. Cheng, P. Du, J. Rogers, and G. O'Grady, "High-resolution mapping of gastric slow wave recovery profiles: biophysical model, methodology and demonstration of applications," *Am. J. Physiol. Gastrointest. Liver Physiol.*, vol. 313, no. 3, pp. G265–G276, 2017.

[21] J. D. Hunter, "Matplotlib: a 2D graphics environment," *Comput. Sci. Eng.*, vol. 9, no. 3, pp. 90–95, 2007.

[22] G. O'Grady, T. Wang, P. Du, T. R. Angeli, W. J. E. P. Lammers, and L. K. Cheng, "Recent progress in gastric arrhythmia: pathophysiology, clinical significance and future horizons," *Clin. Exp. Pharmacol. Physiol.*, vol. 41, no. 10, pp. 854–862, 2014.

[23] P. Du, A. Hameed, T. R. Angeli, C. Lahr, T. L. Abell, L. K. Cheng, and G. O'Grady, "The impact of surgical excisions on human gastric slow wave conduction, defined by high-resolution electrical mapping and in silico modeling," *Neurogastroenterol. Motil.*, vol. 27, no. 10, pp. 1409–1422, 2015.

[24] M. Potse, A. C. Linnenbank, and C. A. Grimbergen, "Software design for analysis of multichannel intracardial and body surface electrocardiograms," *Comput. Methods Programs Biomed.*, vol. 69, no. 3, pp. 225–236, 2002.

[25] M. Potse, A. C. Linnenbank, and C. A. Grimbergen, "Automated generation of isochronal maps in the presence of activation block," *Int. J. Bioelectromagn.*, vol. 4, no. 2, pp. 115–116, 2002.

[26] N. Paskaranandavadivel, J. Gao, P. Du, G. O'Grady, and L. K. Cheng, "Automated classification and identification of slow wave propagation patterns in gastric dysrhythmia," *Ann. Biomed. Eng.*, vol. 42, no. 1, pp. 177–192, Jan. 2014.

[27] T. R. Angeli, P. Du, N. Paskaranandavadivel, A. Hall, S. J. Asirvatham, G. Farrugia, L. K. Cheng, and G.

O'Grady, "High-resolution electrical mapping of porcine gastric slow-wave propagation from the mucosal surface," *Neurogastroenterol. Motil.*, vol. 29, no. 5, p. e13010, 2016.

[28] R. Berry, N. Paskaranandavadivel, P. Du, M. L. Trew, G. O'Grady, J. A. Windsor, and L. K. Cheng, "A novel retractable laparoscopic device for mapping gastrointestinal slow wave propagation patterns," *Surg. Endosc.*, vol. 31, no. 1, pp. 477–486, 2016.

[29] T. R. Angeli, G. O'Grady, N. Paskaranandavadivel, J. C. Erickson, P. Du, A. J. Pullan, I. P. Bissett, and L. K. Cheng, "Experimental and automated analysis techniques for high-resolution electrical mapping of small intestine slow wave activity," *J. Neurogastroenterol. Motil.*, vol. 19, no. 2, pp. 179–191, 2013.

[30] T. R. Angeli, G. O'Grady, P. Du, N. Paskaranandavadivel, A. J. Pullan, I. P. Bissett, and L. K. Cheng, "Circumferential and functional re-entry of in vivo slow-wave activity in the porcine small intestine," *Neurogastroenterol. Motil.*, vol. 25, no. 5, pp. e304-314, 2013.

[31] W. J. E. P. Lammers, B. Stephen, and S. M. Karam, "Functional reentry and circus movement arrhythmias in the small intestine of normal and diabetic rats," *Am. J. Physiol. Gastrointest. Liver Physiol.*, vol. 302, no. 7, pp. G684-689, Apr. 2012.

[32] W. J. E. P. Lammers, L. Ver Donck, J. A. J. Schuurkes, and B. Stephen, "Longitudinal and circumferential spike patches in the canine small intestine in vivo," *Am. J. Physiol. Gastrointest. Liver Physiol.*, vol. 285, no. 5, pp. G1014-1027, Nov. 2003.

[33] J. C. Erickson, R. Velasco-Castedo, C. Obioha, L. K. Cheng, T. R. Angeli, and G. O'Grady, "Automated algorithm for GI spike burst detection and demonstration of efficacy in ischemic small intestine," *Ann. Biomed. Eng.*, vol. 41, no. 10, pp. 2215–2228, Apr. 2013.